

Please Read the Abstract

By

Abstract Writer

Submitted to the graduate degree program in Department of People who read Abstracts and the Graduate Faculty of the University of Kansas in partial fulfillment of the requirements for the degree of Doctor of Philosophy.

Committee members

MEMBER 1, Chairperson

MEMBER 2, Occasional Visitor

MEMBER 3

MEMBER 4, The One Who Never Answers Email

The One with an Extra Long Name

The Fifth Beatle

Date defended: October 02, 2016

The Thesis Committee for Abstract Writer certifies
that this is the approved version of the following thesis :

Please Read the Abstract

MEMBER 1, Chairperson

Date approved: October 06, 2016

Abstract

Acknowledgements

Contents

1	Nuclear Physics in Ultra-relativistic Heavy-Ion Collisions	1
1.1	The Standard Model	1
1.2	Quantum Electrodynamics	2
1.3	Quantum Chromodynamics	2
1.4	QCD Experiments	4
1.5	Deep Inelastic Scattering	4
1.6	Ultra-peripheral Heavy-Ion Collisions	6
2	Diffraction Dijet Photoproduction	8
2.1	Factorization	8
2.2	Wigner Distribution	11
3	The Experiment	14
3.1	Large Hadron Collider	14
3.2	Compact Muon Solenoid	14
3.2.1	Tracker	15
3.2.1.1	Pixel Tracker	17
3.2.1.2	Strip Tracker	17
3.2.2	Electromagnetic Calorimeter	17
3.2.3	Hadronic Calorimeter	19
3.2.3.1	Hadronic Forward Calorimeters	21
3.2.4	Muon Detector	21
3.2.5	Zero Degree Calorimeter	22

3.2.6	Particle Flow Algorithm	22
4	Beam Radiation and Luminosity	24
4.1	van de Meer Scanning	25
5	Triggering	26
6	Data Analysis	28
7	Systematic Uncertainties	29
8	Results and Conclusions	30
A	My Appendix, Next to my Spleen	32

List of Figures

1.1	QCD Coupling Constant vs. Q^2	3
1.2	Collision Cross Section vs Bjorken-x, theory and data	5
1.3	(a.) electromagnetic field of stationary charge (b.) eletromagnetic field of boosted charge	6
2.1	Feynman diagrams for coherent jet photoproduction in (a.) lepton-proton collisions and (b.) Pb-Pb collisions	8
2.2	Ratio of H1 data cross-section to NLO-QCD cross-section	9
2.3	Beam envelope vs. distance to vertex in H1	10
2.4	Subnuclear tomography	11
2.5	Interconnectedness of Parton Distributions	12
2.6	Feynman Diagram of Coherent Dijets in Dipole Framework.	13
3.1	CMS Detector	15
3.2	CMS radial cross-section	16
3.3	Pseudorapidity acceptance of tracker	16
3.4	ECAL components	18
3.5	Ecal energy resolution	18
3.6	Ecal energy resolution	19
3.7	HCAL energy resolution	20
3.8	HCAL Components	20
3.9	Pseudorapidity acceptance of muon detector	22
3.10	Performance of particle flow alorgithm compared to calorimeter readout.	23

5.1	High multiplicity PbPb collision	26
5.2	UPC Upsilon candidate	27

List of Tables

Chapter 1

Nuclear Physics in Ultra-relativistic Heavy-Ion Collisions

1.1 The Standard Model

The Standard Model describes the fundamental particles of the universe in terms of fermions and bosons. Fermions are particles with half-integer spin, while bosons have integer-spin. This difference in spin has far reaching consequences. Fermions must obey the Pauli Exclusion Principle: only one fermion at a time can occupy a given state. However, multiple bosons can simultaneously occupy a specific state.

Among the fermions are the leptons, neutrinos, and quarks. The leptons consist of the electron, muon, and tau, as well as their anti-particles. The leptons are seemingly fundamental: high energy experiments have yet to observe internal lepton-structure. Neutrinos are weakly interacting particles detected primarily through the precise measuring of missing transverse energy in the products of particle collisions. Quarks are the constituent particles of baryons, which contain three valence quarks, and mesons, which contain two valence quarks. In addition to the valence quarks are the sea quarks, which appear and disappear as quark-antiquark pairs within hadrons. The hadrons are particles made of quarks and gluons.

The behavior of fundamental particles is best described within the framework of quantum field theory (QFT). QFT defines a Lagrangian for fundamental particles. This Lagrangian then predicts the outcome of particle collisions. Different terms in the Lagrangian correspond to the various interactions between particles. The Standard Model Lagrangian can be broken down into three basic terms:

$$\mathcal{L}_{StandardModel} = \mathcal{L}_{QED} + \mathcal{L}_{QCD} + \mathcal{L}_{Higgs} + \dots, \quad (1.1)$$

The QED and QCD Lagrangians will be the most important in what follows. Feynman rules are derived from the Lagrangian. Particularly important for the Feynman rules are the coupling constants for the electromagnetic force and strong-nuclear force.

1.2 Quantum Electrodynamics

Quantum electrodynamics (QED) is a theory of electromagnetic interaction in terms of relativistic quantum field theory. QED addresses three specific processes: photon motion, electron motion, and the emission, or absorption, of a photon by an electron. To do this, first a Lagrangian is established based on Maxwell's laws and quantum mechanics. The photon constitutes a spin-1 solution to Maxwell's equations. Likewise, electrons are described, at non-relativistic scales, by the Schrodinger equation, at relativistic scales by the Dirac equation. This Lagrangian is used to calculate the scattering amplitude associated with Feynman diagrams: pictorial representations of how particles interact.

The QED coupling constant is approximately $1/137$ at perturbative scales. However, at small scales, i.e. non-perturbative momentum transfers Q^2 , the coupling constant increases.

$$\alpha_{QED}(Q^2) = \frac{\alpha_{em}}{(1 - \frac{\alpha_{em}}{3\pi}) \ln(\frac{Q^2}{m^2})}, \quad (1.2)$$

1.3 Quantum Chromodynamics

The quarks are a family of fermions that compose the baryons and the mesons. Baryons consist of three quarks in a color neutral state, while mesons consist two quarks in a color neutral state. "Color" in this context refers to the six kinds of strongly-interacting charge available to quarks: red and anti-red, blue and anti-blue, and green and anti-green. Color charge has no relation to optical phenomena, but provides a useful analogy for the stable combinations of quarks. The net

color-charge of a baryon or meson is "white".

Gluons are the QCD analogues of the photons in QED. Gluons are spin-1 and massless, but unlike photons, which do not carry electromagnetic charge, gluons carry strongly-interacting charge: color. Color comes six varieties: red, antired, blue, antiblue, green, and antigreen.

Unlike QED, the QCD coupling increases with distance. Fig.1.1 shows the running of the QCD coupling with Q^2 . This has the practical consequence of the strong-interactions being stronger in high momentum transfer collisions. The direct results of the running QCD coupling are the dual phenomena of asymptotic freedom and color confinement. At large distances, string tension describes the binding force of the quarks. At short distances, however, Coulomb-like interactions dominate.

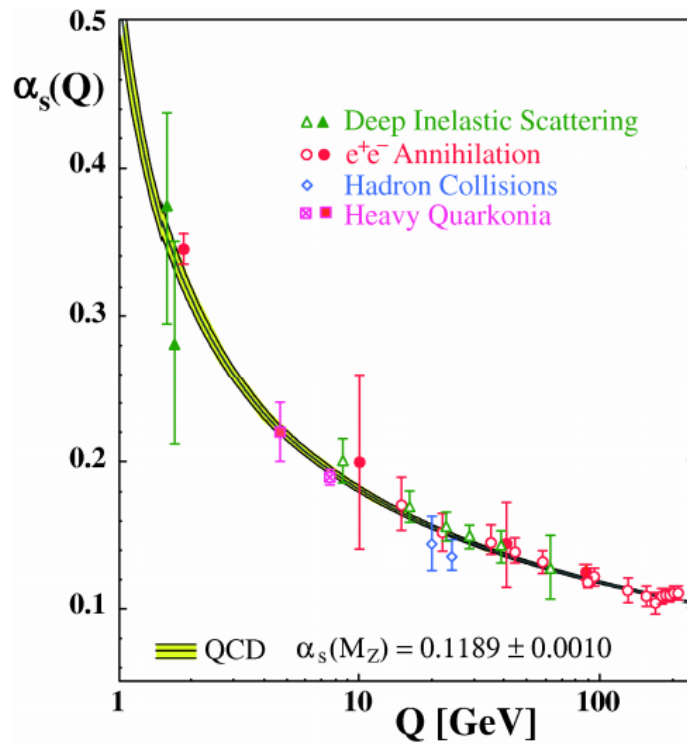


Figure 1.1: QCD Coupling Constant vs. Q^2

Within the nucleus, a proton can be thought of as a bubble in a vacuum. Debye screening exerts a pressure on the proton. This pressure is responsible for the size of the proton.

$$\alpha_{QCD}(Q^2) = \alpha_s(Q^2) = \frac{4\pi}{(11 - \frac{2}{3}n_f)\ln(\frac{Q^2}{\Lambda_{QCD}^2})}, \quad (1.3)$$

1.4 QCD Experiments

Scattering experiments are the basic tool for exploring the nucleus. The Large Hadron Collider (LHC) is capable of reaching heavy-ion collision energies of up to 7 TeV per nucleon-nucleon. The higher the energy, the more experiments can probe the nuclear phase-space diagram. Momentum transferred, expressed as Q^2 , is an important quantity for characterizing QCD measurements. In addition to Q^2 , Bjorken-x, also known as Bjorken-scaling is necessary to describe the nuclear phase space. Bjorken-x represents the momentum fraction of partons.

At the turn of the century, Ernst Rutherford probed the gold atom by bombarding a gold sheet with alpha-particles (helium nuclei). The angular distribution of the scattered alpha-particles demonstrates that the mass of the atom is concentrated in a small volume, i.e, the atom is mostly empty space. Further experiments revealed that the atomic nuclei consisted of separate positively and neutrally charged particles: protons and neutrons.

The modern understanding of subnuclear physics is based on results from three laboratories: Lawrence Berkeley National Laboratory (LBNL), Brookhaven National Laboratory (BNL), and CERN. Fixed target experiments hinted at the existence of a quark gluon plasma, but the collision energies were too low for this state to last.

Collider experiments are capable of reaching much higher energies than fixed target experiments because of relativistic effects.

1.5 Deep Inelastic Scattering

Deep inelastic scattering commonly refers to the scattering of a leptons off hadrons. Experiments at HERA focused on electron-proton collisions. In these collisions, the electron was used as a source of photons and neutrinos. When these particles scatter off the proton, the dependence of the

collision cross section, on momentum transfer and scattering angle of the source electron, reflects the structure of the proton. These experiments provided the first evidence of two phenomena: the parton model and Bjorken-scaling.

The parton model, first proposed by Richard Feynman, posits that hadrons in general, and nucleons in specific, are made of more fundamental constituent particles which may or may not be the quarks implied by the SU(3) symmetry. In addition to the quarks, the partons also include any field quanta associated with nuclear forces. In time, these field quanta are dubbed "gluons".

"Scaling" is an interpretation of the data from deep inelastic scattering (DIS). First proposed by James Bjorken, scaling is reflected in the incoherence of photon-proton interactions at photon energies above $1 \text{ GeV}/c$. Predictions from perturbative QCD are in good agreement with DIS data from HERA, as seen in .1.2.

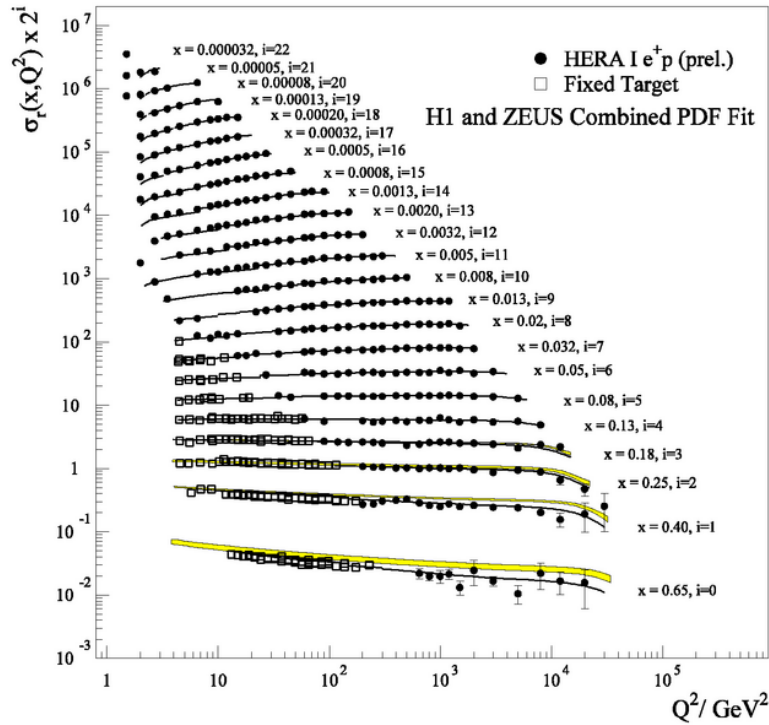


Figure 1.2: Collision Cross Section vs Bjorken-x, theory and data

Soft processes compose the low momentum transfer, typically gluon-gluon interactions during a collision.

1.6 Ultra-peripheral Heavy-Ion Collisions

Similar to the Rutherford experiment, in heavy-ion collisions the scattered particles carry information about the internal structure of the nucleus.

The Rutherford experiment has the three components that still characterize high-energy nuclear experiments: a probe, a medium, and a signal. Alpha particles probe the medium of the gold atom, and the angular distribution of scattered alpha particles signals the internal structure of the atom.

Ultra-peripheral collisions occur at impact parameters greater than the sum of the heavy-ion radii. In these collisions, hadronic interactions are strongly suppressed while photonuclear activity is enhanced proportional to the square of the nuclear charge. The electromagnetic field of an incoming heavy-ion, from the perspective of a target, is equivalent to a flux of virtual photons; fig.1.3 illustrates the Lorentz contraction of the field of a boosted charge.

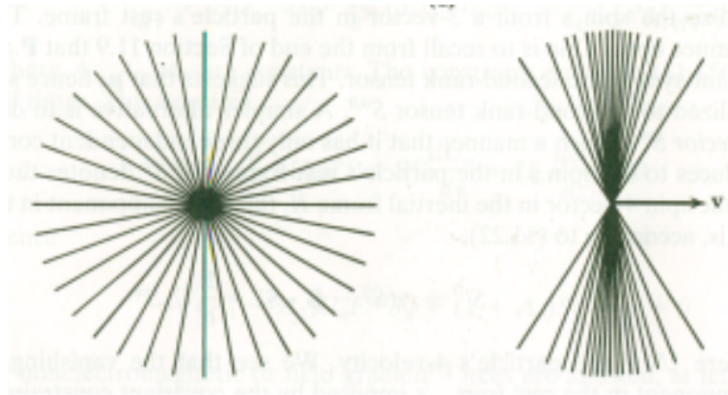


Figure 1.3: (a.) electromagnetic field of stationary charge (b.) electromagnetic field of boosted charge

The Weizsacker-Williams approximation (WWA) calculates the density of photons, about the nucleus, as a function of energy. WWA is a semi-classical formulation. Maxwell's equations are solved for a stationary point charge boosted to an ultra-relativistic velocity. In the target's frame, the Fourier transform of the source field is taken. The Fourier frequency modes are interpreted through the quantum mechanical equation of photon energy.

Gluons are the particle exchanged in strong interactions. However, gluons themselves carry color charge. By analogy, photons transmit the electromagnetic force, but do not themselves have

an electric charge.

When a quark is scattered from a nucleus, the strong interaction gathers potential energy until the threshold for quark production is passed, at which point an anti-quark is generated to screen the ejected quark.

QCD factorisation describes the diffractive-photoproduction dijet cross-section as the convolution of the partonic cross-section with the diffractive parton distributions. However, factorisation only describes H1 data if the resolved-photon contribution is suppressed.

The photoproduction cross-section is proportional to the gluon distribution. At low momentum transfer, photons interact electromagnetically, i.e. directly, with partons. High energy photons possess a hadronic structure.

Chapter 2

Diffractive Dijet Photoproduction

2.1 Factorization

Diffractive dijet photoproduction is not describable in perturbative QCD. For coherent processes the photon energy is small, and therefore the wavelength is large compared to the size of the nucleus. At these large distances, there isn't a hard scale, and so perturbation calculations cannot be done. Gluon splitting interactions dominate the low Bjorken- x partons. QCD collinear factorization describes these soft interactions via the convolution of parton cross sections, taken from perturbative QCD, and diffractive parton distribution functions, taken from experiment.

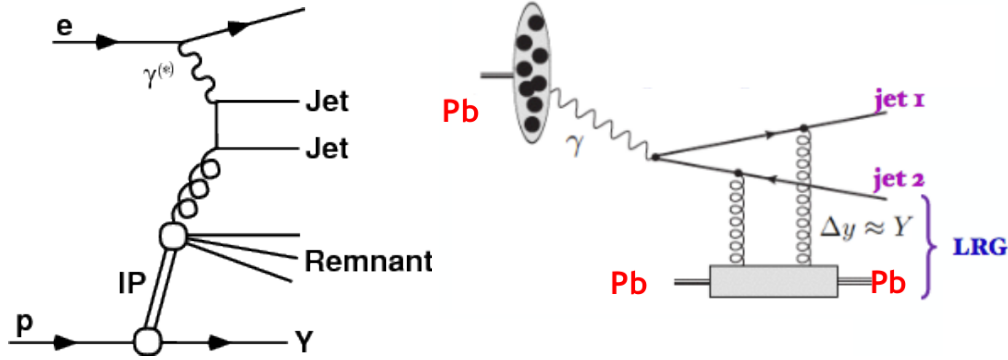


Figure 2.1: Feynman diagrams for coherent jet photoproduction in (a.) lepton-proton collisions and (b.) Pb-Pb collisions

In electron-hadron collisions, diffractive photoproduction is characterized by the presence of a large rapidity gap in the final state and an intact nucleus. The Feynman diagram of electroproduction in lepton-hadron collisions is similar to that of photoproduction in ultraperipheral collisions, as seen in fig.2.1. The diffractive dijet cross section is expressed by the convolution of partonic

cross sections $d\hat{\sigma}$ and diffractive PDFs $f_{i/p}^D$.

$$d\sigma(ep \rightarrow e + 2jets + X' + p) = \sum_i \int dt \int dx_{\mathbb{P}} \int dz_{\mathbb{P}} d\hat{\sigma}_{ei \rightarrow 2jets}(\hat{s}, \mu_R^2, \mu_F^2) \times f_{i/p}^D(z_{\mathbb{P}}, \mu_F^2, x_{\mathbb{P}}, t), \quad (2.1)$$

In the proton-vertex factorisation hypothesis, the dependence on $x_{\mathbb{P}}$ and $|t|$ is factored out of the dependence on μ_F^2 and $z_{\mathbb{P}}$. Furthermore, $f_{i/p}^D$ is sum of contributions from the Pomeron and Reggeon:

$$f_{i/p}^D(z_{\mathbb{P}}, \mu_F^2, x_{\mathbb{P}}, t) = f_{\mathbb{P}/p}(x_{\mathbb{P}}, t) f_{i/\mathbb{P}}(z_{\mathbb{P}}, \mu_F^2) + n_{\mathbb{R}} f_{\mathbb{R}/p}(x_{\mathbb{P}}, t) f_{i/\mathbb{R}}(z_{\mathbb{P}}, \mu_F^2), \quad (2.2)$$

Lepton-hadron collisions were performed at HERA and measured by the H1 experiment. These experiments reported a value for the total diffractive photoproduction cross section that is double that predicted by QCD collinear factorization; fig.2.2 compares the cross-section of H1 data to that predicted by NLO-QCD. Diffractive events were selected for using rapidity gaps or the presence of leading protons in the very forward proton spectrometer (VFPS).

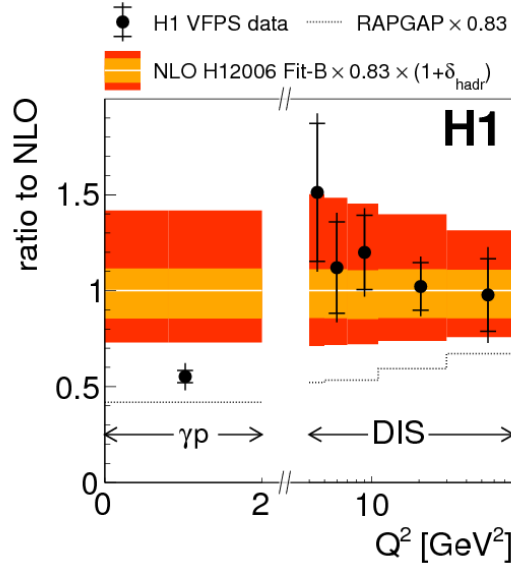


Figure 2.2: Ratio of H1 data cross-section to NLO-QCD cross-section

H1 used the Very Forward Proton Spectrometer (VFPS) to trigger on low Q^2 protons. The

VFPS consists of two Roman Pots located 218 m and 222 m from the H1 interaction-point in the forward direction. The VFPS can detect protons scattered at very low transverse momentum, corresponding to $0.008 < x_P < 0.028$ and $|t| < 0.6$. Each of the Roman Pots contains layers of scintillating fibers, which are covered by a layer of scintillator tiles. The fibers readout to photomultipliers, and the tiles both shield from radiation and trigger on protons. The track efficiency of VFPS is a remarkable 96%, and the background contamination is kept at 1% , making the detector excellent for studying diffractive events. Fig.2.3 shows the $|t|$ coverage of the Forward Proton Spectrometer (FPS) and VFPS.

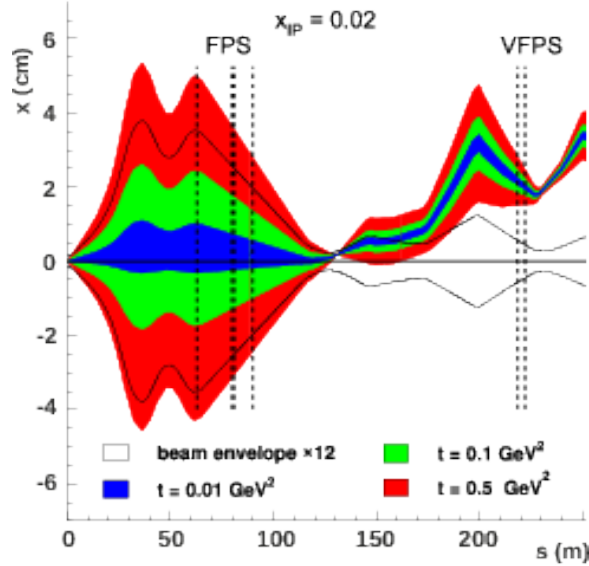


Figure 2.3: Beam envelope vs. distance to vertex in H1

The H1 data was compared to predictions based on NLO-QCD convoluted with diffractive parton distribution functions (DPDFs) from HERA inclusive diffractive deep-inelastic scattering (DDIS) data. For diffractive pp collisions the high transverse momentum jets yield a hard scale for perturbative QCD.

2.2 Wigner Distribution

One can use the Wigner distribution to tomographically image the internal structure of the nucleus. The nucleus manifests different structures at varying momentum fractions; specifically, small momentum fractions exhibit gluon saturation (fig.2.4).

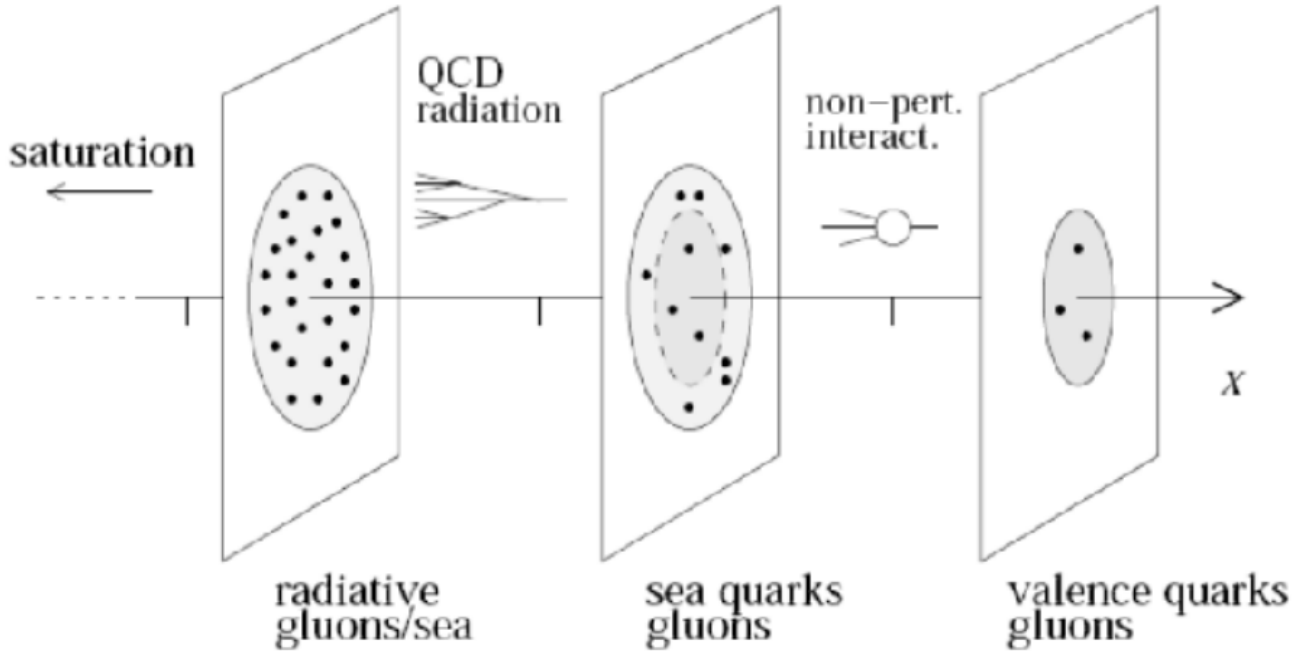


Figure 2.4: Subnuclear tomography

The quantum field theory lagrangian of the strong interaction is relatively simple, but because of confinement and asymptotic freedom the hadronic bound states are too complex for an analytic solution. Furthermore, collider experiment data requires a quantitative interpretation to be useful. The gap between QCD and heavy-ion data is bridged using the parton model, which considers hadrons as composed of quarks and gluons. Parton density functions (PDFs) model the longitudinal momentum distribution of the partons. PDFs are supplemented by transverse momentum distributions (TMDs) and generalized parton distributions (GPDs). In addition to transverse momentum, GPDs describe the transverse spatial distribution. TMDs and GPDs are derived from the final state particles of a collision. Markus Diehl maps the relationship between various distribution

functions in fig.2.5.

The Wigner distribution is a quantum phase space distribution that describes small- x gluons. Specifically, by considering the color dipole scattering amplitude, the angular correlation of the nucleon recoil momentum and the dijet transverse momentum can provide a three-dimensional, tomographic image of the gluons within a high energy nucleus. This tomographic image takes the form of a Wigner distribution, which contains all the information of both TMDs and GPDs without violating the uncertainty principle. Specifically, the angular correlation directly measures the Fourier transform of the gluons. This is possible because the dipole amplitudes are functions of the impact parameter, and because collinear factorization holds.

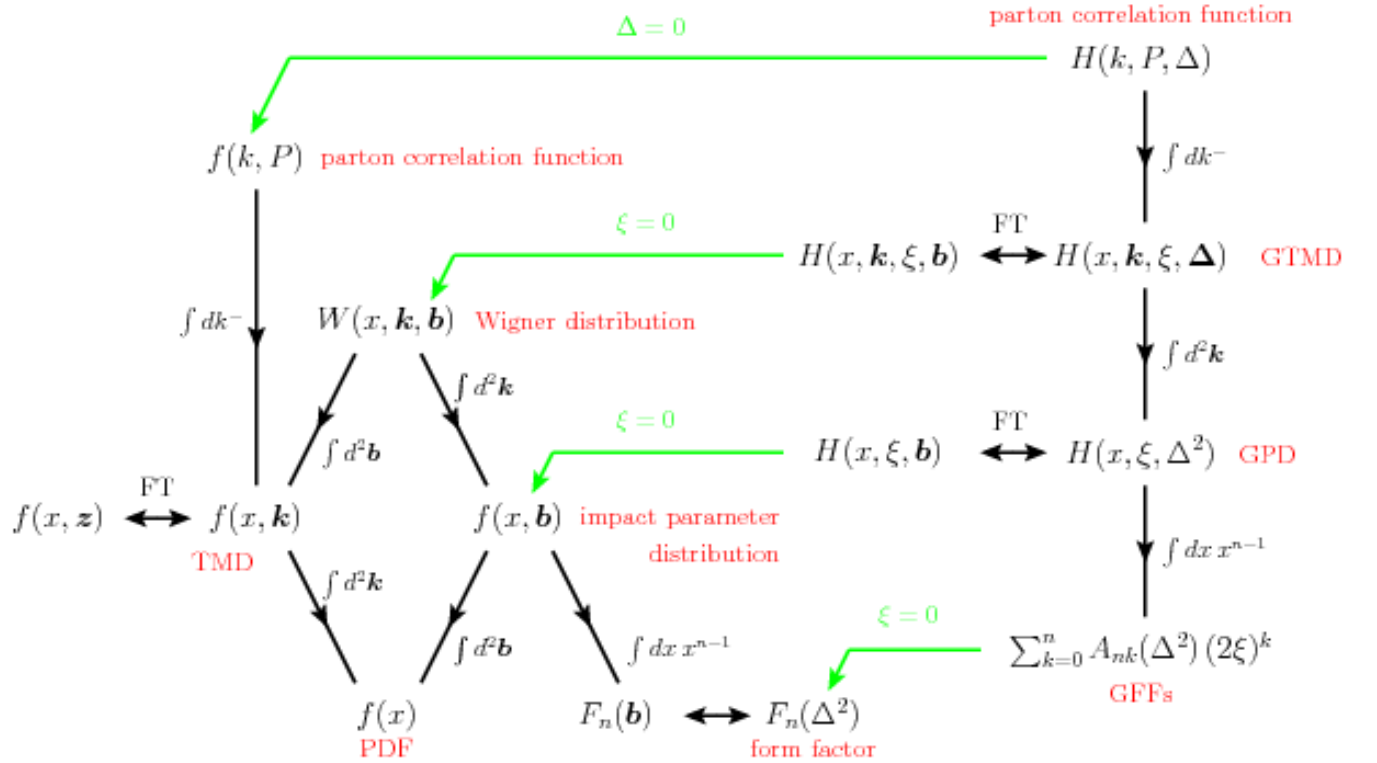


Figure 2.5: Interconnectedness of Parton Distributions

TMDs and GPDs manifest non-perturbative QCD effects. The Wigner distribution, at this scale, reflects the relationship between the position and momentum of partons. Integrating the Wigner function over the transverse distance yields the TMD, while integrating over transverse momentum yields a GPD with spatial information.

Yoshitaka Hatta uses the dipole framework to show that the azimuthal angular correlations of coherent dijets are generated by the underlying gluon Wigner distribution. Furthermore, these correlations are consistent with predictions based on standard collinear factorization. Relevant kinematic variables are mapped in the fig.2.6.

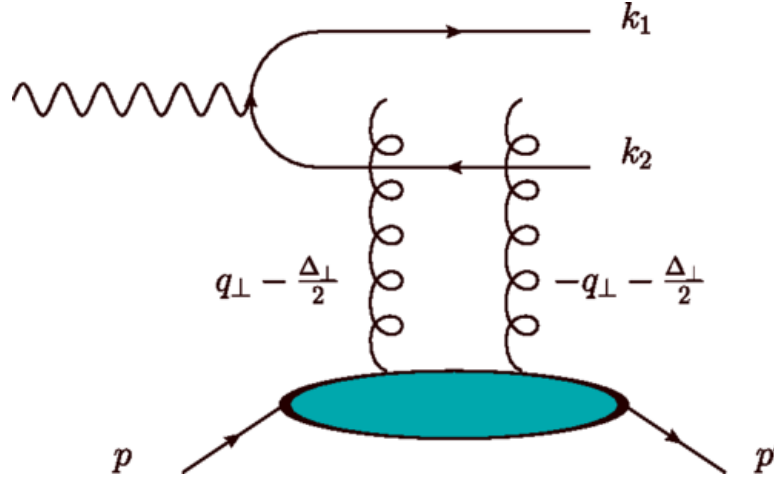


Figure 2.6: Feynman Diagram of Coherent Dijets in Dipole Framework.

Chapter 3

The Experiment

3.1 Large Hadron Collider

The Large Hadron Collider (LHC) has a radius of approximately 27 kilometers. As of this writing, it is the largest machine ever constructed. The initial purpose of the LHC was to discover the Higgs boson, but it is capable of investigating a variety of other physics phenomena, such as dark matter, extra-dimensions, and heavy-ion physics.

The beams are accelerated along a circular path using radio frequency cavities, gaining energy with each revolution. LHC is a hadron collider, meaning it is designed to collide particles made of quarks and gluons. The proton-proton, proton-Pb, and Pb-Pb collision energies are the largest ever probed experimentally. The LHC is a circular collider.

Heavy-ion collisions at LHC produce strongly interacting nuclear matter. The temperature and density of this matter is comparable to the state of the universe only a few milliseconds after the Big Bang.

3.2 Compact Muon Solenoid

The Compact Muon Solenoid (CMS) is a general-purpose particle detector located at Point-5 of the LHC. CMS was designed to precisely measure the momentum of muons. The titular superconducting solenoid magnet was designed to generate a 4 Tesla field, but operates at 3.8 T to increase longevity. This field is homogeneous and parallel to the beam line close to the interaction point. The momentum of a muon is measured from how it deflects when moving through the magnetic

field. Altogether, CMS weighs approximately 12,500 metric tons, with a diameter of 14.6 m and a length of 21.6 meters. Fig.3.1 displays the detector's various sub-systems.

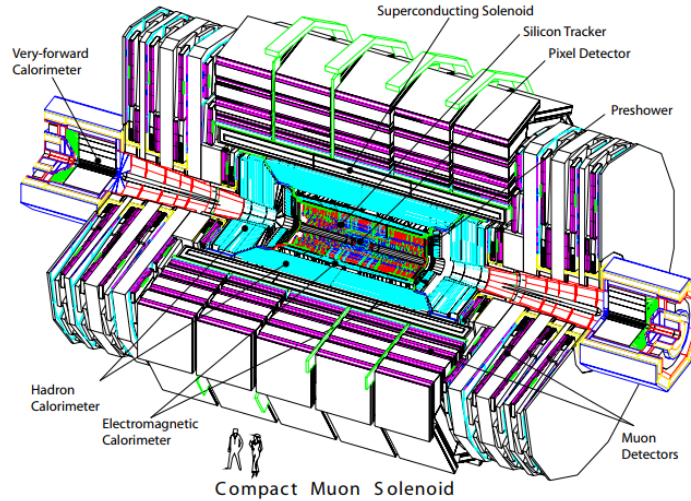


Figure 3.1: CMS Detector

Within the solenoid volume are a silicon pixel and strip tracker, a lead tungsten crystal electromagnetic calorimeter (ECAL), and a brass and scintillator hadron calorimeter (HCAL), each composed of a barrel and two endcap sections. Fig.3.2 radial layering of CMS component systems.

3.2.1 Tracker

The tracker measures the momentum of charged particles via their trajectory through a homogeneous magnetic field. The tracker consists of two units, the pixel tracker and the strip tracker, both of which are made of silicon. A charged particle causes an electrical signal when passing through a silicon pixel or silicon microstrip. CMS reconstructs these electrical signals, taken at specific points of position and time, into tracks. These tracks are accurate to 10 micrometers. The tracker is meant to have a particle pass all the way through it, with only minimal effect particle's trajectory.

The tracker system is designed for high granularity and fast readout, such that each trajectory can be associated with its corresponding bunch crossing. The tracker is resilient enough to

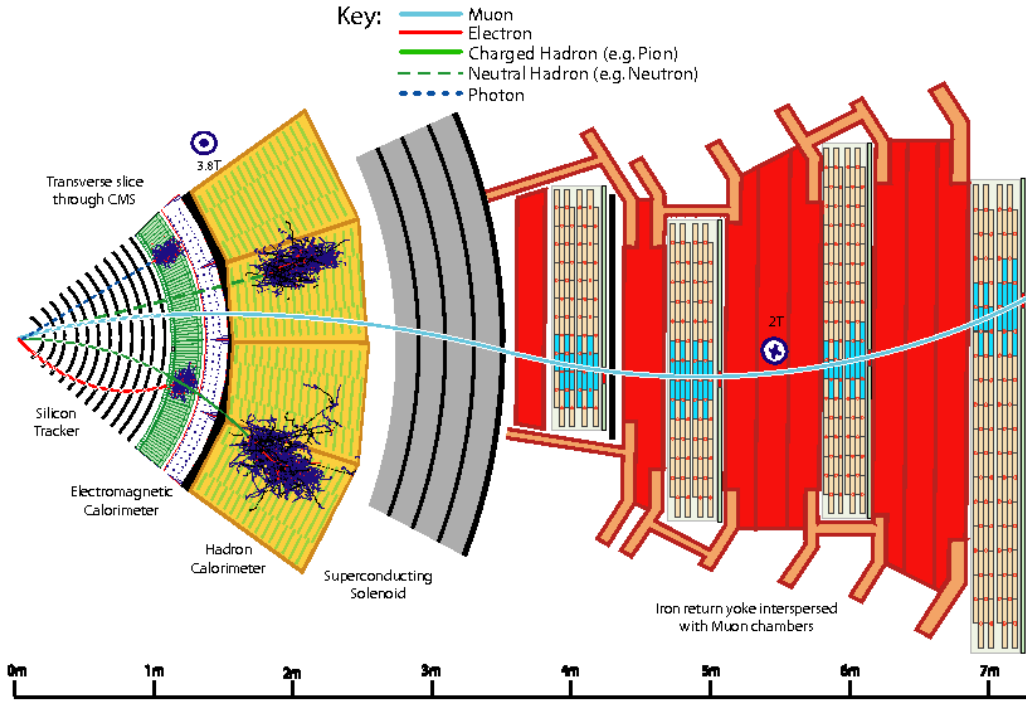


Figure 3.2: CMS radial cross-section

withstand the high flux of particles accompanying every bunch crossing; at design luminosity of $10^{34} \text{cm}^{-2} \text{s}^{-1}$, some 1000 particles will traverse the tracker every 25 ns. However, the mass of the tracker is minimal enough to suppress multiple scattering, off its material, that would distort particle trajectories. These design constraints – resistance and transparency – are satisfied silicon. The tracker has approximately 200m^2 of silicon surface, making it the largest silicon detector ever constructed. The pseudorapidity coverage of the pixel and strip trackers is shown in fig.3.3.

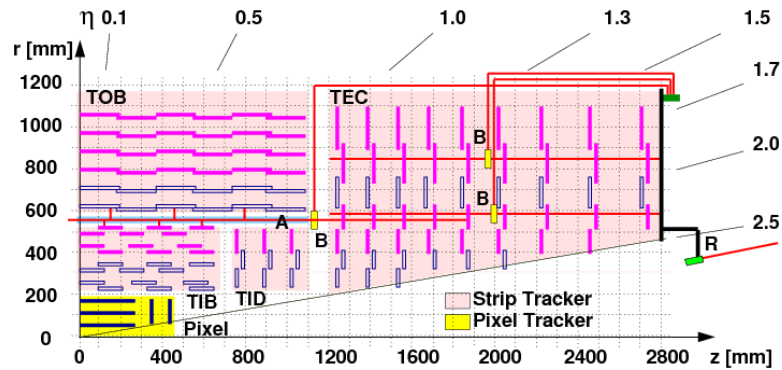


Figure 3.3: Pseudorapidity acceptance of tracker

3.2.1.1 Pixel Tracker

Every silicon-pixel has a corresponding readout chip. The readout chips are soldered through the bump-bonding method. The readout chip amplifies signals from the pixel. The pixel tracker is precise enough to distinguish the vertices of tracks originating from short-lived particles, such as bottomonia. The innermost elements of the pixel tracker come within 4.4 cms of the CMS interaction point. The pixel tracker covers a pseudorapidity range of $|\eta| < 2.5$ with some 66×10^6 separate pixels.

3.2.1.2 Strip Tracker

Outside the pixel tracker are the layers of the strip tracker. They function similar to the components of the pixel tracker, except the strip tracker consists of thin silicon plates. The strip tracker itself can be broken down into four components: the inner barrel layer, the inner endcaps, the outer barrel layer, and the outer endcaps. In total, these layers contain some 9.3×10^6 strips.

3.2.2 Electromagnetic Calorimeter

The Electromagnetic Calorimeter (ECAL) is the dedicated CMS calorimeter for detecting electrons and photons. The calorimeter is comprised of lead tungstate ($PbWO_4$) crystals arranged in cylinder about the beam, including two endcaps, as seen in fig3.4. The granularity of these crystals gives the ECAL excellent energy resolution, angular resolution, and spatial resolution; for example, the ECAL has the resolution suitable for the decay of the Higgs boson into two photons. The ECAL is both hermetic and homogenous.

The data readout is fast enough that CMS can trigger off signals in the ECAL. It takes about 25 ns for an ECAL hit to scintillate 80 percent of its lights, putting the calorimeter's rate on the same scale as the bunch crossing. Scintillation in the crystals activates photodetectors that transmit information to the L1 trigger. In the barrel these photodetectors are avalanche photodiodes (APDs). The endcaps use vacuum phototriodes (VPTs). ECAL's energy resolution, as a function of energy,

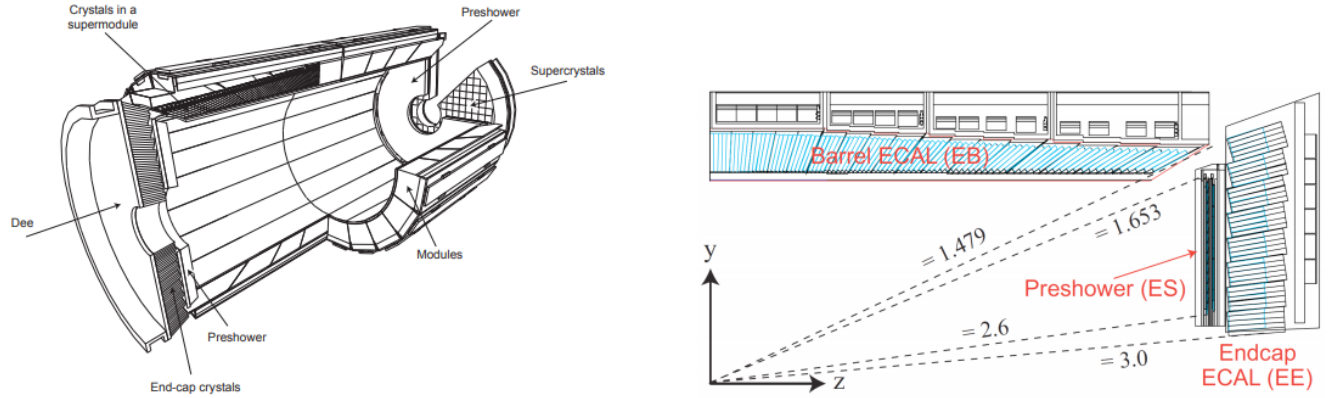


Figure 3.4: ECAL components

is given by fig.3.5. The resolution increases with energy because, at large energies, parton showers become more similar as their random fluctuations average-out.

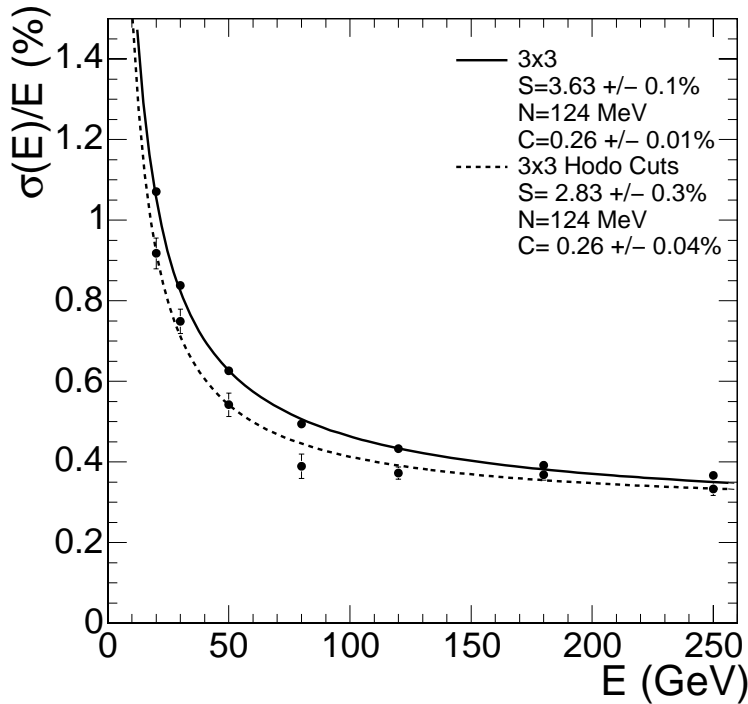


Figure 3.5: Ecal energy resolution

In CMS trigger development, "EG" triggers fire based on energy deposits in the ECAL; fig.3.6 gives the EG trigger energy resolution. This energy comes primarily from electrons and photons. When these particles strike a tungstate crystal, the particle shower size is approximately that of the crystal. Electrons are distinguished from photons by the correlation of track to ECAL energy. The

L1 trigger does not fire on tracks, which are reconstructed at the HLT level. Thus, L1 EG triggers do not distinguish between electrons and photons.

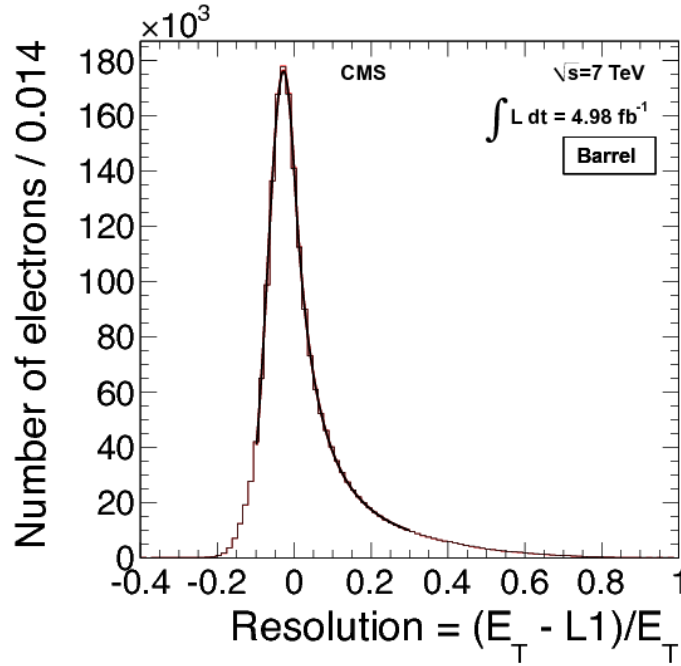


Figure 3.6: Ecal energy resolution

3.2.3 Hadronic Calorimeter

The Hadronic Calorimeter (HCAL) is the next layer outside the ECAL. The HCAL is a sampling calorimeter, meaning that it absorbs particles and measures their energy and momentum via scintillation. HCAL has such a large acceptance that it can indirectly observe non-interacting particles such as neutrinos. The HCAL is designed to be hermetic, so that imbalances of momentum and energy can be precisely measured. Fig.3.7 plots the HCAL's energy resolution; note that the reso-

lution changes with $|\eta|$.

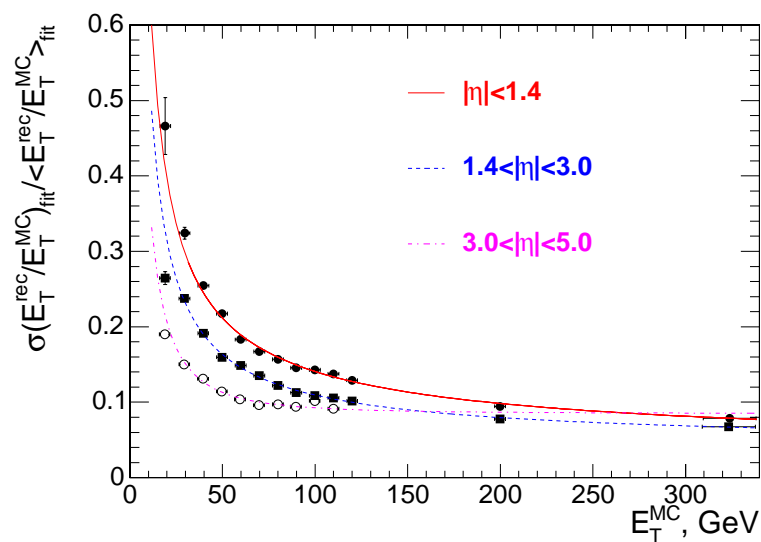


Figure 3.7: HCAL energy resolution

There are four sub-sections of the HCAL: the inner barrel (HB) and the outer barrel (HO), two endcaps (HE), and two forward calorimeters (HF). The HF are the most relevant to this analysis because of their use in triggering on non-hadronic events. Fig.3.8 shows the HCAL energy resolution.

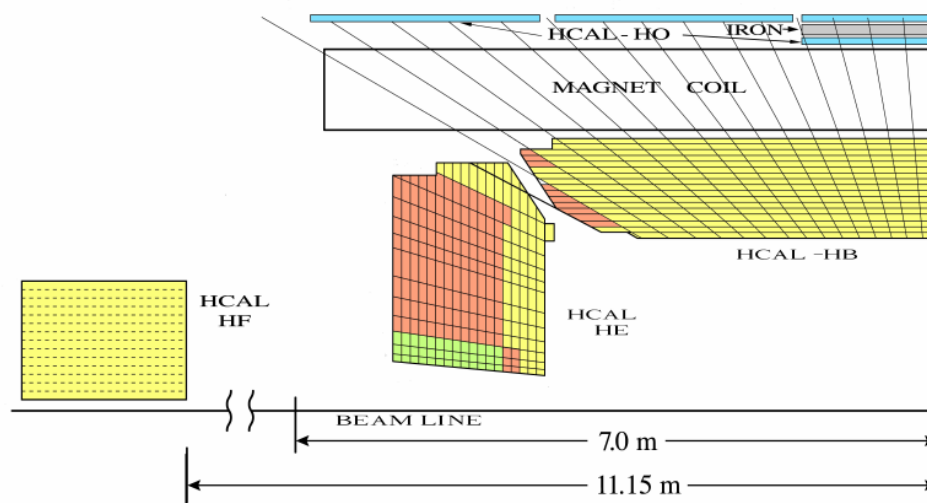


Figure 3.8: HCAL Components

3.2.3.1 Hadronic Forward Calorimeters

The Hadronic Forward Calorimeters (HF) absorbs the greatest portion of energy from collisions. As named, it is located in the forward region ($3.0 < |\eta| < 5.2$) of CMS and complements the coverage provided by the barrel and endcap detectors.

HCAL is made of quartz fibers and steel absorbers for maximum radiative resistance. When high energy particles pass through the quartz fibers, these particles are moving faster than the speed of light in the medium, depositing energy that causes particle showers. These showers give off light, in the form of Cherenkov radiation, that the fibers transmit to photomultiplier tubes (PMTs). The PMTs readout to the L1-trigger. Triggering on HF can also be done by vetoing on HF activity.

Hits in the HF are used to measure the instantaneous luminosity of CMS. As shown in fig.3.7, the HF have a finer E_T resolution than the other parts of the HCAL, making it suitable for high precision measurement of luminosity. Furthermore, because HF noise is comparatively small with respect to Minbias HF threshold, the veto of the HF threshold is a reliable measure of HF "emptiness".

3.2.4 Muon Detector

The outermost layer of CMS consists of the muon detectors, as seen in fig.3.9. Muons are particles nearly identical to electrons, except for their mass, which exceeds that of the electron by some two orders of magnitude. High mass particles, like the Higgs boson, often decay into a final state containing muons. The muon detector not only identifies muons, but also measures their momentum. The muon detector has readout fast enough for triggering on muons.

The muon detector consists of three types of component: muon drift tubes (DT), cathode strip chambers (CSC), and resistive plate chambers (RPC). The DTs are gas filled chambers that contain a stretched metal wire. When muons pass through the DT gas, electrons are excited. These electrons escape from the gas atoms and are attracted to the metal wire, which triggers a signal. The CSC, located in the endcaps, operate under similar principles, but contain perpendicular arrays of positively charged and negatively charged wires immersed in gas. The RPC do not use electrode

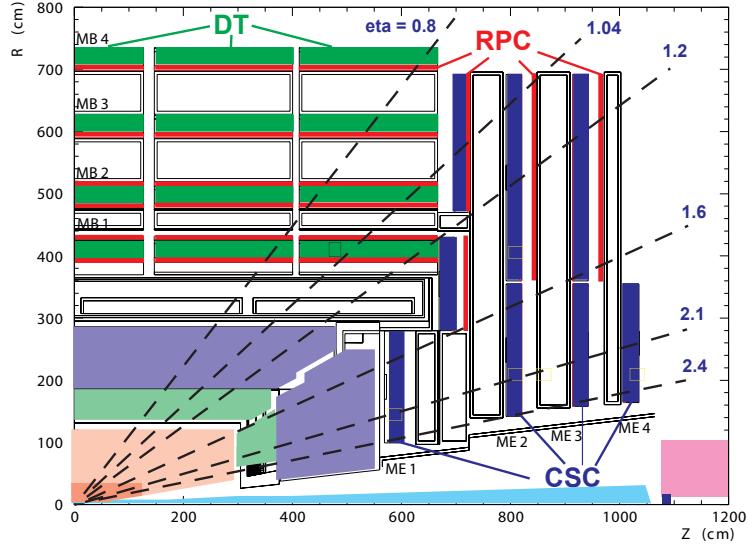


Figure 3.9: Pseudorapidity acceptance of muon detector

wires to detect excited electrons; instead, high-resistivity plates are used as alternating cathodes and anodes.

3.2.5 Zero Degree Calorimeter

The zero degree calorimeters are both sides of CMS, approximately 140 meters from the interaction point. Each ZDC consists of two independent systems: an electromagnetic calorimeter, for detecting very forward photons, and a hadronic calorimeter, for detecting neutrons. Because these neutrons result from the dissociation of nuclei, the ZDC can measure the centrality of heavy-ion collisions. Hadrons in the forward region have energy on the TeV scale, so the ZDC's hadronic calorimeter is made of thick tungsten plates. For a UPC process, the photon emitting nucleus is most likely to remain intact; therefore, ZDC data can the photon direction of a process, and by extension it's energy.

3.2.6 Particle Flow Algorithm

Raw data from the sub-detectors is combined, for data analysis, by the particle-flow (PF) algorithm. The PF takes the data about tracks in the tracker and energy deposits in the calorimeter,

and uses them to reconstruct physics-related data objects, like jets, and to identify specific particles, such as photons and muons. The PF also identifies missing energy and momentum for use in neutrino studies. These data objects are stored in a format similar to that of conventional MC event generators. CMS gains significant jet reconstruction efficiency via the PF. At low transverse momentum, PF reconstructs jets at nearly twice the resolution of HCAL and ECAL. This increase in efficiency comes from the PF integrating in track data with the calorimeter tower data. Fig.3.10 compares the performance of the PF algorithm to the calorimeter reconstruction.

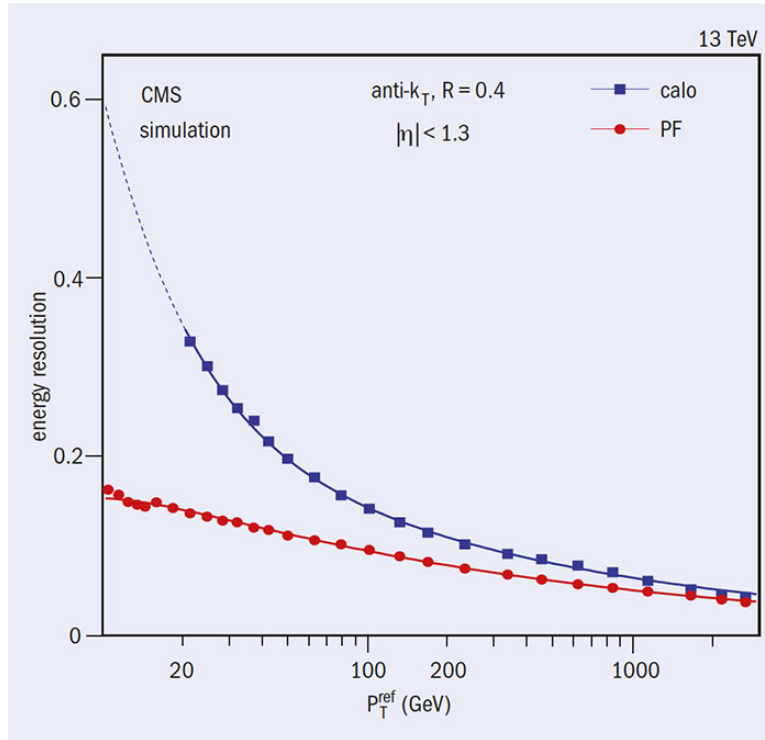


Figure 3.10: Performance of particle flow algorithm compared to calorimeter readout.

Chapter 4

Beam Radiation and Luminosity

One of the most important quantities measured by CMS is luminosity. Luminosity is necessary to convert the number of events detected, for a given channel, into a collision cross-section. Collision cross-sections are among the primary observables predicted by theoretical physics, specifically quantum field theory. For particle physics, the collision cross-section of a process is typically measured through the relation:

$$\sigma = \frac{R}{L}, \quad (4.1)$$

Where σ is the cross-section, R is the rate at which the process occurs per collision, and L is the luminosity.

There are two kinds of CMS luminometer: online and offline. Online luminometers readout the luminosity per bunch in real time. As of 2015 there are three online luminometers: the pixel luminosity telescope (PLT), the HF, and the beam conditions monitor (BCM1f). There is a high-rate, independent data-acquisition system for each of the online luminometers. Offline luminometers measure the rate of reconstructed objects. The primary offline luminometer is the pixel tracker. In general, the offline luminometers have better stability over time. CMS (2010)

The online and offline luminometers complement each other for high precision data analysis. Specifically, the offline data can be used to calibrate out imperfections in the online data.

In addition to these hardware luminometers, CMS can use physics processes as luminosity benchmarks. For example, other experiments have measured the Z-boson cross-section to a high accuracy and high precision. Comparing this cross-section to the Z-boson mass-peak, in CMS

data, provides a cross-check to the delivered luminosity.

4.1 van de Meer Scanning

The luminometers of CMS produce signals proportional to the instantaneous luminosity of the LHC beam. However, these signals need to be properly calibrated with respect to a known visible cross-section for each luminometer. This calibration is accomplished via Van de Meer scanning. The opposing beams of LHC are moved back and forth in the transverse plane. During the scan, the detector response is measured as a function of beam displacement. The beam widths are calculated from Gaussian fits to the detector response. The visible cross-section of the luminometer in question is then derived from the width of the beams, and acts as the calibration of the detector response.

Chapter 5

Triggering

CMS uses a two-tiered triggering system. The first tier, the L1 trigger, is hardware based. The second tier, the high-level trigger (HLT), is software based. The L1 trigger receives raw data from the calorimeters and the muon detectors; this determines when the tracker will readout data. The raw data from the tracker, calorimeters, and muon detectors is then passed on to a computer farm running the HLT menu. The HLT then performs a simplistic reconstruction of the raw data into physics objects useful for analysis: jets, tracks, and identifiable particles. If an event passes the HLT, the raw data is permanently stored in preparation for a more complex reconstruction.

The 2015 UPC triggers were for low multiplicity events and low transverse momentum events. Typical heavy-ion collisions are high multiplicity events. Fig.5.1 is an event display of one of the first heavy-ion collisions at CMS in 2010.

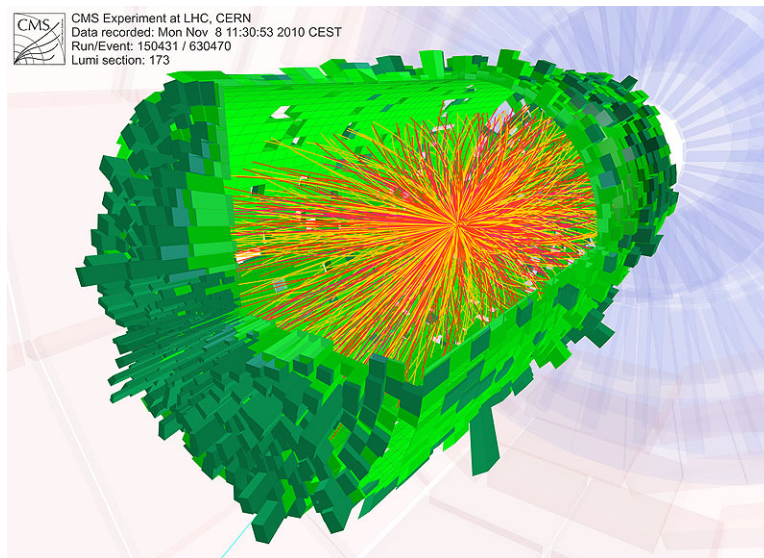


Figure 5.1: High multiplicity PbPb collision

Fig.5.2 is the event display of a UPC upsilon candidate.

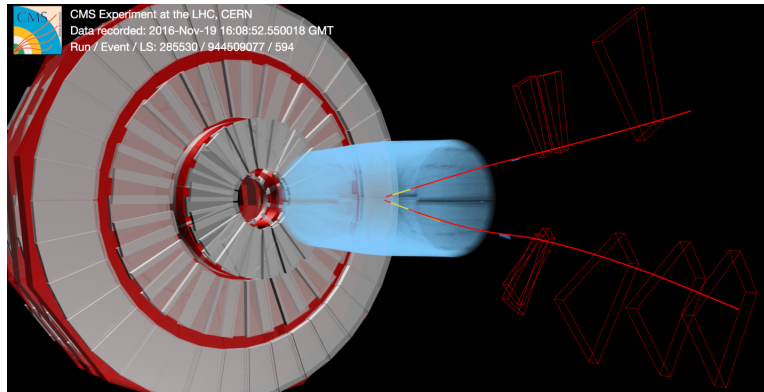


Figure 5.2: UPC Upsilon candidate

For this analysis, the L1 trigger applies two selections. First, the L1 checks that at least one of the HF is empty. This is the most important part of the trigger in so far as it suppressed the hadronic contamination of the dataset. Then, if there is at least 5 GeV of energy deposited in the ECAL, the event passes to the HLT.

Low multiplicity events are difficult to distinguish from background. To compensate, the HLT in turn requires that there be at least once reconstructed track from the pixel tracker, to make sure that there are particles that will be reconstructed by the complete tracker. Only the pixel tracker is used for these HLTs to increase the speed of reconstruction while decreasing needed computer cycles.

Chapter 6

Data Analysis

Chapter 7

Systematic Uncertainties

Chapter 8

Results and Conclusions

References

(2010). Measurement of CMS Luminosity.

Aaron, F. D. et al. (2010). Diffractive Dijet Photoproduction in ep Collisions at HERA. *Eur. Phys. J.*, C70, 15–37.

Aaron, F. D. et al. (2011). Measurement of the cross section for diffractive deep-inelastic scattering with a leading proton at HERA. *Eur. Phys. J.*, C71, 1578.

Andreev, V. et al. (2015). Diffractive Dijet Production with a Leading Proton in ep Collisions at HERA. *JHEP*, 05, 056.

Benaglia, A. (2014). The CMS ECAL performance with examples. *JINST*, 9, C02008.

Bethke, S. (2007). Experimental tests of asymptotic freedom. *Prog. Part. Nucl. Phys.*, 58, 351–386.

Chekanov, S. et al. (2009). Deep inelastic scattering with leading protons or large rapidity gaps at HERA. *Nucl. Phys.*, B816, 1–61.

Crittenden, J. A. (1997). Exclusive production of neutral vector mesons at the electron - proton collider HERA.

Guzey, V. & Klasen, M. (2016a). A fresh look at factorization breaking in diffractive photoproduction of dijets at HERA at next-to-leading order QCD. *Eur. Phys. J.*, C76(8), 467.

Guzey, V. & Klasen, M. (2016b). Diffractive dijet photoproduction in ultraperipheral collisions at the LHC in next-to-leading order QCD. *JHEP*, 04, 158.

Appendix A

My Appendix, Next to my Spleen

There could be lots of stuff here